

Structure, Dielectric and Multiferroic Properties of $\text{Bi}_{0.85}\text{Nd}_{0.15}\text{Fe}_{0.98}\text{Zr}_{0.02}\text{O}_3$ in Ba and Ti Co-Doping

Lizhu Zeng

Southwest University

Yuming Lu

Southwest University

Lujia Zhang

Southwest University

Xin Gong

Southwest University

Jianfeng Tang

Southwest University

Guannan Li (✉ liguannan@swu.edu.cn)

Southwest University <https://orcid.org/0000-0002-4432-6657>

Research Article

Keywords: dielectric, multiferroic, BaTiO₃

Posted Date: March 12th, 2021

DOI: <https://doi.org/10.21203/rs.3.rs-283706/v1>

License:  This work is licensed under a Creative Commons Attribution 4.0 International License.

[Read Full License](#)

Abstract

Multiferroic $(1-x)\text{Bi}_{0.85}\text{Nd}_{0.15}\text{Fe}_{0.98}\text{Zr}_{0.02}\text{O}_3-x\text{BaTiO}_3$ ($x = 0, 0.275, 0.3, 0.325, 0.35, 0.375, 0.4$) ceramics were synthesized by the conventional solid state reaction method. X-ray diffraction studies confirm the phase transition from rhombohedral perovskite structure to pseudocubic structure with the introduction of BaTiO_3 . The results of the refinement indicate the BaTiO_3 is successfully doped into the crystal lattice. The microstructure analysis shows that the average grain size increases with the introduction of BaTiO_3 . An increase in remanant polarization has been achieved at room temperature as the BaTiO_3 concentration increasing. A greatly reduced leakage current density of about two orders of magnitude is observed in $x = 0.375$ ($J = 2.4 \times 10^{-7} \text{ A/cm}^2$) ceramic. The dielectric properties have been enhanced by the addition of BaTiO_3 , which is attributed to the reduction in Fe^{2+} ions and oxygen vacancies. Due to the grain effect and structure transition caused by the doping of BaTiO_3 , the magnetization reveals a slight decrease while the coercive field for $x = 0.325$ ($H_c = 1785.8 \text{ Oe}$) increases to 6.4 times of the undoped ceramic.

1 Introduction

Multiferroics have received significant attention in recent years because of their interesting intrinsic physics and potential applications. This kind of material always exhibits the simultaneous existence of two or more ferroic properties like ferroelectric, ferromagnetism and ferroelasticity, which show tremendous application foregrounds such as actuators, energy harvesting devices, memory elements and sensors.^[1-4] As a room temperature multiferroic material, BiFeO_3 (BFO) is one of the most studied systems in current years.^[5-7] In bulk form, BFO possesses a distorted perovskite structure with rhombohedral symmetry (space group $R3c$).^[8] With the high anti-ferromagnetic Néel temperature ($T_N = 643 \text{ K}$) and ferroelectric Curie temperature ($T_C = 1103 \text{ K}$), the BFO based ceramics make it possible to be applied at a high operating temperature.^[9, 10]

The bulk BiFeO_3 is always characterized by high leakage current and weak magnetoelectric properties, which limit its use for making multifunctional devices. The reasons are chiefly as follows: Firstly, single-phase BFO ceramics are difficult to synthesize because of their narrow phase stability temperature range. Secondly, the main reasons for low electrical resistivity in BFO ceramics are the reduction of Fe ions from Fe^{3+} to Fe^{2+} and the formation of oxygen vacancy during the sintering process, which requires charge compensation.^[11-14] Also, the G-type anti-ferromagnetism of BFO is one of the main obstacles to obtain the larger magnetoelectric (ME) effect, which hinders its effective application.^[15] To improve the multiferroic properties of BFO ceramics, many efforts have been done including varieties of synthetic techniques, chemical substitution, and formation of solid solution with other ABO_3 perovskite materials.^[3, 16-19]

Among the potentially multiferroic solid solutions, BiFeO₃-BaTiO₃ displays a high T_c and magnetoelectric coupling performance.^[20–23] The BFO-based solid solution can effectively prevent the generation of the second phase and increase the resistivity of the samples. In the BiFeO₃-BaTiO₃ solutions, the A and B sites both have different valence ions, which makes it possible for relaxor ferroelectrics.^[24] Despite many studies on the BiFeO₃-based solid solutions that have been done, a systematical understanding of structure-property correlation in these systems is still lacking. Buscaglia et al. have closely studied the magneto-electric properties of (1- x) BiFeO₃- x BaTiO₃ ceramics.^[21] According to Makhdoome et al., ferromagnetism enhancement was detected in Ba-doped BFO ceramics, in which the coercive field and the remnant magnetization increased with the increasing of Ba concentration.^[25] Moreover, Hu et al. have reported that B-site doping with Ti ions can decrease the density of leakage current and improve ferroelectric properties.^[26] Additionally, the replacement of Ti⁴⁺ altered the bond angle of the Fe-O-Fe and distorted FeO₆ octahedra, resulting in an enhancement of the magnetization.^[27, 28]

Previous studies suggest that Nd³⁺ doping can effectively improve the piezoelectric properties, long range ferroelectricity and magnetic response. The substitution of smaller Nd³⁺ (radius = 0.983 Å) ions for larger Bi³⁺ (radius = 1.03 Å) ions in BFO can produce single-phase ferromagnetism, showing enhanced spontaneous magnetization.^[29] Besides, the valence of Zr⁴⁺ ion is higher than that of Fe³⁺ ion, the substitution of Zr⁴⁺ at Fe-site can provide extra electrons to fill the oxygen vacancies. With the nonmagnetic element Zr doping, the spiral magnetic spin structure is suppressed.^[30] Hence, a new compound containing Bi_{0.85}Nd_{0.15}Fe_{0.98}Zr_{0.02}O₃ and BaTiO₃ components are synthesized to realize the enhancement in dielectric and multiferroic properties through the conventional solid-state sintering method. The structure, morphology, multiferroic, dielectric and magnetic properties are also investigated in relation to the BaTiO₃ content in detail.

2 Experimental

Polycrystalline ceramics (1- x)Bi_{0.85}Nd_{0.15}Fe_{0.98}Zr_{0.02}O₃- x BaTiO₃ (x = 0, 0.275, 0.3, 0.325, 0.35, 0.375 and 0.4) were fabricated by the solid-state reaction method. The high purity ($\geq 99.9\%$) Bi₂O₃, Nd₂O₃, Fe₂O₃, ZrO₂, BaCO₃ and TiO₂ were used in a stoichiometric ratio as the precursor powders. All the powders were mixed thoroughly via ball milling (Mini-Mill Pulverisette 23, Fritsch) for 3 h at a speed of 30r/s. The mixture was dried and calcined at 800°C for 2 h. The calcined powder was applied to a second ball milling for another 1.5 h at a speed of 30 r/s. The resulting powders added with polyvinyl alcohol (PVA) solution (5 wt.%) were pressed into discs with a dimension of 10 mm in diameter and 1 mm in thickness under a 20 MPa pressure. After removal of the binder at 500°C, all the specimens were sintered at 910–1080°C in the air for 2 h.

The crystal structure of the ceramics was studied by an X-ray diffractometer (XRD, 6100, Shimadzu, Japan) with Cu-K α radiation (λ = 1.54056 Å). Rietveld refinement of the XRD data was performed using the Fullprof software package. Microstructures of the ceramics were performed by using a scanning

electron microscopy (SEM, JSM 6610, Jeol, Japan). Before conducting the electrical test, the ceramics was first ground to 0.5 mm thick sheets, then the two surfaces were coated with silver paste. All the resulting ceramics were sintered at 600°C for 10 minutes and the electrodes were finally prepared. The temperature-dependence dielectric constant (ϵ_r) and dielectric loss ($\tan\delta$) of the ceramics were characterized by using a programmable furnace with an LCR analyzer (E4980AL, Keysight, USA) at 1 kHz and 100 kHz. The ferroelectric properties and the leakage current density were measured at room temperature using a ferroelectric analyzer (TF analyzer 2000E, aix ACCT, Germany). The surface chemical state of the prepared ceramics was analyzed by an X-ray photoelectron spectroscopy (XPS, Thermo ESCALAB 250XI) with Al K α radiation. The magnetic properties were tested by using the Physical Property Measurement System (PPMS, Quantum Design, USA).

3 Results And Discussion

3.1 Crystal structure

Figure 1(a) shows the room temperature XRD patterns of $(1-x)\text{Bi}_{0.85}\text{Nd}_{0.15}\text{Fe}_{0.98}\text{Zr}_{0.02}\text{O}_3-x\text{BaTiO}_3$ (BNFZ- x BT, $x = 0, 0.275, 0.3, 0.325, 0.35, 0.375, 0.4$) ceramics in the 2θ range of $20^\circ - 80^\circ$. The XRD pattern of $\text{Bi}_{0.85}\text{Nd}_{0.15}\text{Fe}_{0.98}\text{Zr}_{0.02}\text{O}_3$ ceramic agrees very well with those earlier reports, pointing out that the rhombohedral $R3c$ symmetry.^[31] Due to the volatility of the Bi element, an impurity peak is detected in the undoped sample indicating the formation of the secondary phase of $\text{Bi}_2\text{Fe}_4\text{O}_9$ (asterisk in Fig. 1 (a)). Fortunately, the introduction of BaTiO_3 effectively stabilizes the BFO structure and inhibits the generation of the second phase.^[30] Fig. 1(b) shows the (104) and (110) peaks shift toward low angles slightly with the content of BaTiO_3 increasing and then superpose together forming one diffraction peak (110) for the doped samples in the 2θ range of $31^\circ - 33^\circ$, which suggests that the ceramics undergo a phase transition.^[32] The same situation is found in the 2θ range of $44^\circ - 48^\circ$ in Fig. 1(c).^[33]

Detailed analysis of the crystal structure has been performed using the Rietveld method. Figure 2(a-b) shows the results of the Rietveld refinement for $x = 0$ and 0.275 ceramics. The refinements of the other samples are found to have the similar results with $x = 0.275$ sample. According to the results, the crystal structure of the sample changed from rhombohedral phase $R3c$ to a pseudo-cubic structure.^[34] The difference curves at the bottom are nearly flat and the reliable factors are reasonable indicating the results of the refinement are credible. The structure parameters of all the ceramics are shown in Table 1. It is obvious to see the lattice parameters increase with the increase of BaTiO_3 content ($0.275 \leq x \leq 0.4$). This is because the radius of Bi^{3+} (1.03 Å) is much smaller than that of Ba^{2+} (1.35 Å) while the ionic radius of Fe^{3+} (0.64 Å) is close to that of Ti^{4+} (0.608 Å). The expansion of the lattice also indicates that the BaTiO_3 successfully entered into the crystal lattice.^[34]

Table 1
The lattice parameters obtained by Rietveld refinement for $(1-x)$
 $\text{Bi}_{0.85}\text{Nd}_{0.15}\text{Fe}_{0.98}\text{Zr}_{0.02}\text{O}_3-x\text{BaTiO}_3$ ($x = 0, 0.275, 0.3, 0.325, 0.35, 0.375$ and 0.4)
ceramics.

x	$a/\text{Å}$	$b/\text{Å}$	$c/\text{Å}$	$V/\text{Å}^3$	$\rho/\text{g}\cdot\text{cm}^{-3}$	R_{wp}	χ^2
0	5.5876	5.5876	13.8372	374.141	8.12	17.4	1.94
0.275	3.9729	3.9729	3.9791	62.809	7.55	11.7	1.54
0.3	3.9759	3.9759	3.9826	62.957	7.48	13.3	1.53
0.325	3.9781	3.9781	3.9839	63.017	7.43	11.2	1.63
0.35	3.9825	3.9825	3.9845	63.192	7.36	11.4	1.47
0.375	3.9859	3.9859	3.9845	63.303	7.30	13.9	1.42
0.4	3.9881	3.9881	3.9848	63.376	7.25	14.9	1.62

3.2 Microstructure

The microstructural morphologies of $(1-x)\text{Bi}_{0.85}\text{Nd}_{0.15}\text{Fe}_{0.98}\text{Zr}_{0.02}\text{O}_3-x\text{BaTiO}_3$ ($x = 0, 0.275, 0.3, 0.325, 0.350, 0.375$ and 0.4) ceramics performed by SEM are shown in Fig. 3. The average grain size shown in Fig. 3(h) was measured using the IMAGE-J by the linear intercept method. The relative density of BNFZ - x BT ceramics are 96.25%, 94.08%, 96.44%, 96.64%, 99.80%, 99.04% and 97.99% for $x = 0, 0.275, 0.300, 0.325, 0.35, 0.375$ and 0.4 specimens, respectively. As the doping ratio increasing, the relative density of the ceramics is improved while excessive BaTiO_3 content deteriorates the density. It can be seen that some obvious pores appear in Fig. 4(a) and 4(b), but not found in the other ceramics. The SEM results indicate that introduction of BaTiO_3 into BNFZ has an effect on promoting grain growth and densification. One can observe that the average grain size increases as the BaTiO_3 content increasing. With further increasing content of BaTiO_3 , the average grain size of samples seems not to determine a further increase.

3.3 Ferroelectric properties

Figure 4(a) shows the P - E loops of $(1-x)\text{Bi}_{0.85}\text{Nd}_{0.15}\text{Fe}_{0.98}\text{Zr}_{0.02}\text{O}_3-x\text{BaTiO}_3$ ($x = 0, 0.275, 0.3, 0.325, 0.35, 0.375$ and 0.4) ceramics measured under an electric field of 50 kV/cm . Figure 4(b) shows the BaTiO_3 content dependence of the remnant polarization $2P_r$ of all the ceramics. Compared with the pure BiFeO_3 , the ferroelectric properties are improved by the Nd^{3+} and Zr^{4+} co-doping in $\text{Bi}_{0.85}\text{Nd}_{0.15}\text{Fe}_{0.98}\text{Zr}_{0.02}\text{O}_3$. As shown in Fig. 4(a) and 4(b), with an further increase in the content of BaTiO_3 , the values of $2P_r$ are $0.496 \mu\text{C/cm}^2, 0.782 \mu\text{C/cm}^2, 0.922 \mu\text{C/cm}^2, 0.966 \mu\text{C/cm}^2, 1.108 \mu\text{C/cm}^2, 1.146 \mu\text{C/cm}^2$ and $1.524 \mu\text{C/cm}^2$, respectively. It can be seen that the P_r and average grain size have the same change trend which is consistent with the studies before.^[35] The ceramics with large grains always exhibit better ferroelectric characteristics. With the grain size increasing, the grain boundary of the sample decreases, which makes

the ferroelectric domain more easily flipped under the external electric field.^[36] In addition, when BaTiO₃ is doped, the Ti-O bonds are established and the Fe-O bonds are disrupted. Owing to the long-range Ti displacement, the samples with more content of BaTiO₃ show better ferroelectric properties.

Figure 5 shows the leakage current density (J) versus the applied electric field of all the ceramics. Compared with the previous studies, all the samples have a low leakage current density which is less than 5.9×10^{-5} A/cm² for pure BFO ceramics at an applied electric field of 6 kV/cm.^[37] It is evident that the leakage current density decreases with BaTiO₃ introduced. A significant decrease for approximately two orders of magnitude is observed for $x = 0.375$ sample. The improved J value might be associated with the decrease of oxygen vacancies caused by the addition of BaTiO₃. The electrons trapped in the oxygen vacancies can be easily activated for conduction by an applied electric field, thus increasing the J value.^[8] With the BaTiO₃ substitution, the Ba-O bond in the ceramics is hard to destroy compared to the Bi-O bond which greatly inhibits the volatility of Bi element. Besides, the improved morphology and structure transition are also beneficial to suppress the leakage current density. With a further increase of x , the J value increases a little. This is because that the extra electrons introduced by the excess BaTiO₃ join in the electronic conduction.

To further understand the roles of Bi and Fe valences on the ferroelectric properties, a detailed X-ray photoelectron spectra analysis for Bi 4*f* and Fe 2*p* lines of all the ceramics is shown in Fig. 6. As shown in Fig. 6(a), the peaks around 158.3 and 163.7 eV correspond to the Bi 4*f*_{7/2} and Bi 4*f*_{5/2} respectively for all compositions. This indicates that the Bi³⁺ stably exists in the ceramics. The core spectra of the Fe 2*p* spectrum lines are shown in Fig. 6(b). The peak around 709.5 eV corresponds to the state of Fe²⁺ and peaks around 723.5 eV and 711.0 eV correspond to the state of Fe³⁺. As the BaTiO₃ content increases, the percentages of Fe³⁺ ions are 52.3%, 56.8%, 57.2%, 57.5%, 58.2%, 59.0% and 55%, respectively. It is obvious to see that the addition of BaTiO₃ increases the Fe³⁺ concentration which means fewer oxygen vacancies exist in the ceramics. Namely, the Fe²⁺ formation is suppressed, thus facilitating the improvement of resistivity. This result is consistent with those of the ferroelectric property and the leakage current density. The fewer oxygen vacancies can increase the domain-wall mobility which is beneficial to improve the ferroelectric properties.^[38]

3.4 Dielectric properties

The temperature-dependence of dielectric constant (ϵ_r) and dielectric loss ($\tan \delta$) were measured at 1 kHz and 100 kHz of all the samples from room temperature to 400°C shown in Fig. 7. Note that the dielectric constants and the loss $\tan \delta$ at 1 kHz are larger than that measured at 100 kHz. This could be attributed to the different polarization mechanisms which include electronic displacement polarization, space charge polarization and orientation polarization. At higher frequencies, only the electronic displacement polarization is effective to the dielectric constant while all the mechanisms are effective at lower frequencies. Another reason for the decrement in dielectric constant is that the high frequency provides sufficient energy for the electron hopping between Fe²⁺ and Fe³⁺ ions.^[39] In Fig. 7(a), the maximum

dielectric constant is obtained for $x = 0.4$ ceramic at the temperature 329°C (T_m) which corresponds to the Néel temperature (T_N) caused by the magnetic ordering transition from antiferromagnetism to paramagnetism. This phenomenon usually indicates the coupling relationship between the magnetic and the electric order parameters. The anomaly near T_N is always ascribed to the Landau-Devonshire theory of phase transition.^[40, 41] With the increase of BaTiO_3 concentration, the dielectric maximum peak shifts gradually toward higher temperature. Further increasing the frequencies in Fig. 7(b), the T_N is out of the observation range.

As shown in Fig. 7(a) and 7(b), all the dielectric constants present a similar response trend with respect to the temperature and approach a saturated platform except the $x = 0$ sample. Compared with the undoped sample, all the other ceramics exhibit a dielectric relaxation character.^[39, 42] In addition to the broaden peak of the ϵ_r - T peak, the dielectric constant values are slightly decreased and the peak position of ϵ_r also changed toward the high temperature with the frequency increasing.^[43] It is evident from Fig. 7(a) - (d) that the dielectric constant increases and the dielectric loss decreases dramatically as the BaTiO_3 introduced. The improvement can be attributed to the excellent dielectric properties of BaTiO_3 which is caused by the large electronegativity difference and tolerance factor between Ba^{2+} and Ti^{4+} ions.^[44] Another possible cause of the improvement in dielectric property is the oxygen vacancies are suppressed by the addition of BaTiO_3 . The oxygen vacancies produced by Bi volatilization always result in high conductivity and poor dielectric properties. Doping of Ba^{2+} and Ti^{4+} can stabilize the perovskite structure and suppress the defects thus optimize the ϵ_r and $\tan\delta$ value. Simultaneously, the electrons hopping between Fe^{3+} and Fe^{2+} ions are weakened because of the suppression for the valence fluctuation from Fe^{3+} to Fe^{2+} by BaTiO_3 doping, which is in accord with the XPS results shown in Fig. 6.

3.5 Magnetic properties

The magnetization hysteresis loops of $(1-x)\text{Bi}_{0.85}\text{Nd}_{0.15}\text{Fe}_{0.98}\text{Zr}_{0.02}\text{O}_3-x\text{BaTiO}_3$ ($x = 0, 0.275, 0.3, 0.325, 0.35, 0.375$ and 0.4) ceramics for the maximum magnetic field of 30 kOe are shown in Fig. 8. In comparison with the pure BiFeO_3 ceramic,^[45] the $\text{Bi}_{0.85}\text{Nd}_{0.15}\text{Fe}_{0.98}\text{Zr}_{0.02}\text{O}_3$ doped with Nd^{3+} and Zr^{4+} already exhibits weak ferromagnetism with a lower coercivity. Pure BiFeO_3 always presents a G-type antiferromagnetic structure due to the space modulated spin ordering of Fe^{3+} ions^[34]. The substitution of Fe^{3+} ions by the nonmagnetic ion Zr^{4+} generates the unbalance antiferromagnetic structure thus the spiral arrangement of Fe^{3+} is disrupted resulting in net macroscopic magnetization. With further doping of BaTiO_3 , a decrease in magnetization has occurred. The decreased magnetization in Ba^{2+} and Ti^{4+} substituted $\text{Bi}_{0.85}\text{Nd}_{0.15}\text{Fe}_{0.98}\text{Zr}_{0.02}\text{O}_3$ might be caused by the size effect. As shown in Fig. 3(h), the grain size increases as x increasing. The increase in size would decrease the spin canting of magnetic moments at the particle surface, which decreases the Dzyaloshinskii-Moriya (DM) interaction resulting in a lower magnetization.^[46] In addition, with BaTiO_3 doping, the crystal structure transformed from rhombohedral structure to pseudo-cubic structure which has an untilted FeO_6 octahedra. The Fe-O-Fe bond angle is nearly 180° and the strong antiferromagnetic interaction is induced between the

neighboring Fe spins, therefore the magnetization is reduced. After the incorporation of BaTiO₃, the remnant magnetization and coercivity values first increase and then decrease as the BaTiO₃ concentration increases. For $x = 0.325$, the sample obtains the maximum remnant magnetization (0.055 emu/g) and the coercive field ($H_c = 1785.8$ Oe).

4 Conclusions

Polycrystalline specimens of all the ceramics were synthesized by using solid-state reaction method. The merging of doubly split peaks to single ones in data indicated the rhombohedral to pseudo-cubic structure transformation caused by the doping of BaTiO₃. SEM images reveal that the increase in the BaTiO₃ content improves the densification of the ceramics. The maximum value of the average grain size of 3.7 μm ($x = 0.4$) is observed. As increasing the BaTiO₃ content, the value of the remanent polarization ($2P_r$) increases and reaches the maximum value of 1.524 $\mu\text{C}/\text{cm}^2$ for $x = 0.4$ ceramic. The decrease concentration of oxygen vacancy in the $x = 0.375$ sample is confirmed from the XPS results. The leakage current density decreases for approximately two orders of magnitude is observed for $x = 0.375$ ($J = 2.4 \times 10^{-7}$ A/cm²) sample. Dielectric measurements indicate that doped samples exhibit a dielectric relaxation character, the dielectric constant is found to increase and the dielectric loss is decreased with the increase in the concentration of BaTiO₃. The magnetic studies confirm that after the incorporation of BaTiO₃, the remnant magnetization and coercivity values first increase and then decrease as the BaTiO₃ concentration increasing. The H_c are observed maximum value for $x = 0.325$ ceramic.

Declarations

Acknowledgements

This work was supported by the National Natural Science Foundation of China (Grant number 51802270, 51501159) and the Natural Science Foundation of Chongqing, China (Grant number cstc2020jcyj-msxmX0356).

References

1. M. Fiebig, T. Lottermoser, D. Meier, M. Trassin, Nature Reviews Materials **1**, (2016)
2. N.A. Spaldin, R. Ramesh, Nature Materials **18**, 203-212 (2019)
3. C. Tsou, M. Ji, M. Bakhtiary-Noodeh, T. Detchprohm, R.D. Dupuis, S. Shen, IEEE Transactions on Electron Devices **66**, 4273-4278 (2019)
4. W.C. Zheng, D.X. Zheng, Y.C. Wang, D. Li, C. Jin, H.L. Bai, Journal of Magnetism and Magnetic Materials **481**, 227-233 (2019)
5. P. Bai, Y. Zeng, J. Han, Y. Wei, M. Li, Ceramics International **45**, 7730-7735 (2019)

6. N. Wang, A. Jain, Y. Li, F.L. Wang, Y.L. Lu, H. Zhen, Y.G. Wang, F.G. Chen, *Ceramics International* **46**, 3855-3860 (2020)
7. W. Eerenstein, N.D. Mathur, J.F. Scott, *Nature* **442**, 759-765 (2006)
8. M. Muneeswaran, S.H. Lee, D.H. Kim, B.S. Jung, S.H. Chang, J.-W. Jang, B.C. Choi, J.H. Jeong, N.V. Giridharan, C. Venkateswaran, *Journal of Alloys and Compounds* **750**, 276-285 (2018)
9. P. Fischer, M. Polomska, I. Sosnowska, M. Szymanski, *Journal of Physics C: Solid State Physics* **13**, 1931 (2000)
10. R. Palai, R.S. Katiyar, H. Schmid, P. Tissot, S.J. Clark, J. Robertson, S.A.T. Redfern, G. Catalan, J.F. Scott, *Physical Review B* **77**, 014110 (2008)
11. G.L. Yuan, S.W. Or, J.M. Liu, Z.G. Liu, *Applied Physics Letters* **89**, (2006)
12. M. Čebela, D. Zagorac, K. Batalović, J. Radaković, B. Stojadinović, V. Spasojević, R. Hercigonja, *Ceramics International* **43**, 1256-1264 (2017)
13. Y. Gu, J. Zhao, W. Zhang, H. Zheng, L. Liu, W. Chen, *Ceramics International* **43**, 14666-14671 (2017)
14. M.I. Morozov, M.-A. Einarsrud, T. Grande, *Applied Physics Letters* **104**, 122905 (2014)
15. D. Lebeugle, D. Colson, A. Forget, M. Viret, A.M. Bataille, A. Gukasov, *Phys Rev Lett* **100**, 227602 (2008)
16. T. Zheng, J. Wu, *Journal of Alloys and Compounds* **676**, 505-512 (2016)
17. P.C. Sati, M. Kumar, M. Arora, M. Tomar, V. Gupta, *Ceramics International* **43**, 4904-4909 (2017)
18. J.R. Teague, R. Gerson, W.J. James, *Solid State Commun* **8**, 1073-& (1970)
19. A.K. Pradhan, K. Zhang, D. Hunter, J.B. Dadson, G.B. Loiutts, P. Bhattacharya, R. Katiyar, J. Zhang, D.J. Sellmyer, U.N. Roy, Y. Cui, A. Burger, *Journal of Applied Physics* **97**, (2005)
20. Q. Pan, B.-J. Chu, *Chinese Physics B* **29**, (2020)
21. M.T. Buscaglia, L. Mitoseriu, V. Buscaglia, I. Pallecchi, M. Viviani, P. Nanni, A.S. Siri, *Journal of the European Ceramic Society* **26**, 3027-3030 (2006)
22. S.O. Leontsev, R.E. Eitel, *Journal of the American Ceramic Society* **92**, 2957-2961 (2009)
23. S.-C. Yang, A. Kumar, V. Petkov, S. Priya, *Journal of Applied Physics* **113**, (2013)
24. G.A. Samara, *Journal of Physics: Condensed Matter* **15**, R367-R411 (2003)
25. A.R. Makhdoom, S.M. Shah, T. Mahmood, M.J. Iqbal, M.J. Akhtar, M.A. Rafiq, *Journal of Magnetism and Magnetic Materials* **484**, 286-290 (2019)
26. J.-H. Zhu, J.-Q. Dai, J.-W. Xu, X.-Y. Li, *Ceramics International* **44**, 9215-9220 (2018)
27. C.-C. Qiu, Y.-Y. Zhang, X.-S. Lv, Y.-G. Yang, L. Wei, H.-J. Yu, Y.-Y. Hu, H.-D. Zhang, X.-P. Wang, Q.-G. Li, *Journal of Materials Science-Materials in Electronics* **31**, 6394-6397 (2020)
28. M. Sun, L. Bai, W. Ma, Y. Liu, J. Zhang, J. Yang, *ACS omega* **5**, 29292-29299 (2020)
29. D. Wang, M. Wang, F. Liu, Y. Cui, Q. Zhao, H. Sun, H. Jin, M. Cao, *Ceramics International* **41**, 8768-8772 (2015)

30. R. Palai, R. Katiyar, H. Schmid, P. Tissot, S. Clark, J. Robertson, S. Redfern, G. Catalan, J. Scott, *Phys Rev B* **77**, (2008)
31. B.K. Vashisth, J.S. Bangruwa, A. Beniwal, S.P. Gairola, A. Kumar, N. Singh, V. Verma, *Journal of Alloys and Compounds* **698**, 699-705 (2017)
32. L.-F. Zhu, B.-P. Zhang, S. Li, G.-L. Zhao, *Journal of Alloys and Compounds* **727**, 382-389 (2017)
33. N. Zhao, H. Fan, X. Ren, J. Ma, J. Bao, Y. Guo, Y. Zhou, *Ceramics International* **44**, 18821-18827 (2018)
34. S.D. Zhou, Y.G. Wang, Y. Li, H. Wu, L. Zhu, *Ceramics International* **45**, 7210-7216 (2019)
35. D. Lin, Q. Zheng, Y. Li, Y. Wan, Q. Li, W. Zhou, *Journal of the European Ceramic Society* **33**, 3023-3036 (2013)
36. S.D. Zhou, Y. Li, H. Wu, L. Zhu, Y.G. Wang, *Journal of Magnetism and Magnetic Materials* **476**, 472-477 (2019)
37. N. Zhao, H. Fan, X. Ren, J. Ma, J. Bao, Y. Guo, Y. Zhou, *Ceramics International* **44**, 18821-18827 (2018)
38. T. Rojac, M. Kosec, B. Budic, N. Setter, D. Damjanovic, *Journal of Applied Physics* **108**, (2010)
39. B. Vashistha, J. Bangruwa, A. Beniwal, S.P. Gairola, A. Kumar, N. Singh, V. Verma, *Journal of Alloys and Compounds* **698**, (2016)
40. S. Godara, N. Sinha, B. Kumar, *Ceramics International* **42**, 1782-1790 (2016)
41. M. Gowrishankar, D.R. Babu, S. Madeswaran, *Journal of Magnetism and Magnetic Materials* **418**, 54-61 (2016)
42. Q.Q. Wang, C.C. Wang, N. Zhang, H. Wang, Y.D. Li, Q.J. Li, S.G. Huang, Y. Yu, Y.M. Guo, Z.Q. Lin, *Journal of Alloys and Compounds* **745**, 401-408 (2018)
43. T. Wang, J. Hu, H. Yang, L. Jin, X. Wei, C. Li, F. Yan, Y. Lin, *Journal of Applied Physics* **121**, (2017)
44. B.L. Gu, H. Gui, Z.R. Liu, R. Liu, X.W. Zhang, *Journal of Applied Physics* **85**, 2408-2413 (1999)
45. G.L. Song, Y.C. Song, J. Su, X.H. Song, N. Zhang, T.X. Wang, F.G. Chang, *Journal of Alloys and Compounds* **696**, 503-509 (2017)
46. Anju, A. Agarwal, P. Aghamkar, V. Singh, O. Singh, A. Kumar, *Journal of Alloys and Compounds* **697**, 333-340 (2017)

Figures

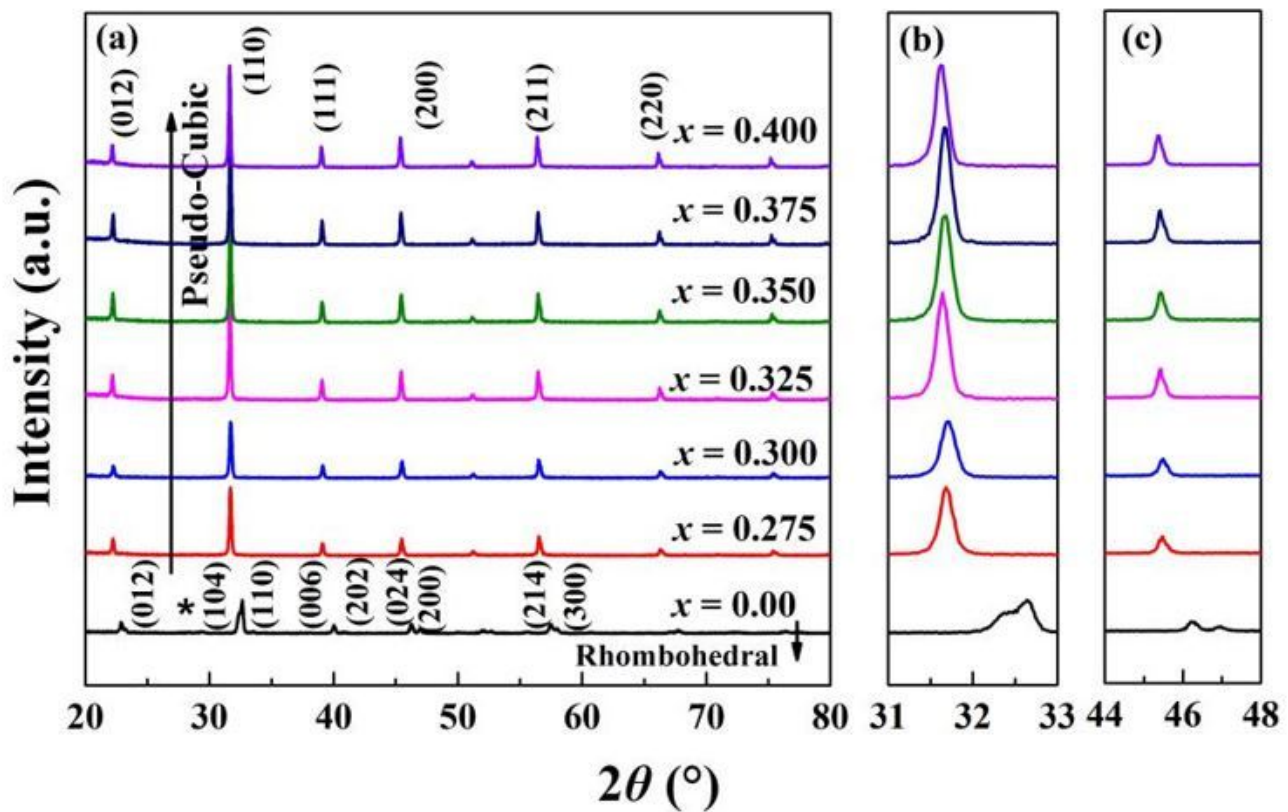


Figure 1

XRD patterns of $(1-x)\text{Bi}_{0.85}\text{Nd}_{0.15}\text{Fe}_{0.98}\text{Zr}_{0.02}\text{O}_{3-x}\text{BaTiO}_3$ ($x = 0, 0.275, 0.3, 0.325, 0.35, 0.375$ and 0.4) solid solutions. (a) $2\theta = 20^\circ - 80^\circ$, (b) $2\theta = 31^\circ - 33^\circ$, (c) $2\theta = 44^\circ - 48^\circ$.

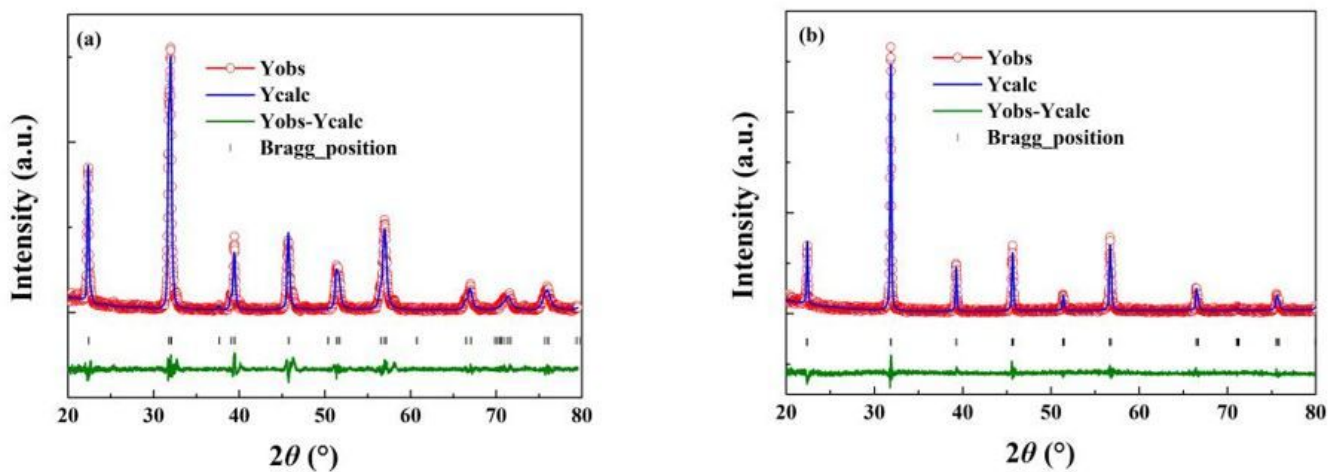


Figure 2

Plot of observed and calculated XRD patterns for $(1-x)\text{Bi}_{0.85}\text{Nd}_{0.15}\text{Fe}_{0.98}\text{Zr}_{0.02}\text{O}_3 - x\text{BaTiO}_3$ ceramics. The short bars indicate the positions of Bragg reflections. The difference plot, $I(\text{obs}) - I(\text{cal})$, is shown in the lower part of the figure: (a) $x = 0$, (b) $x = 0.275$.

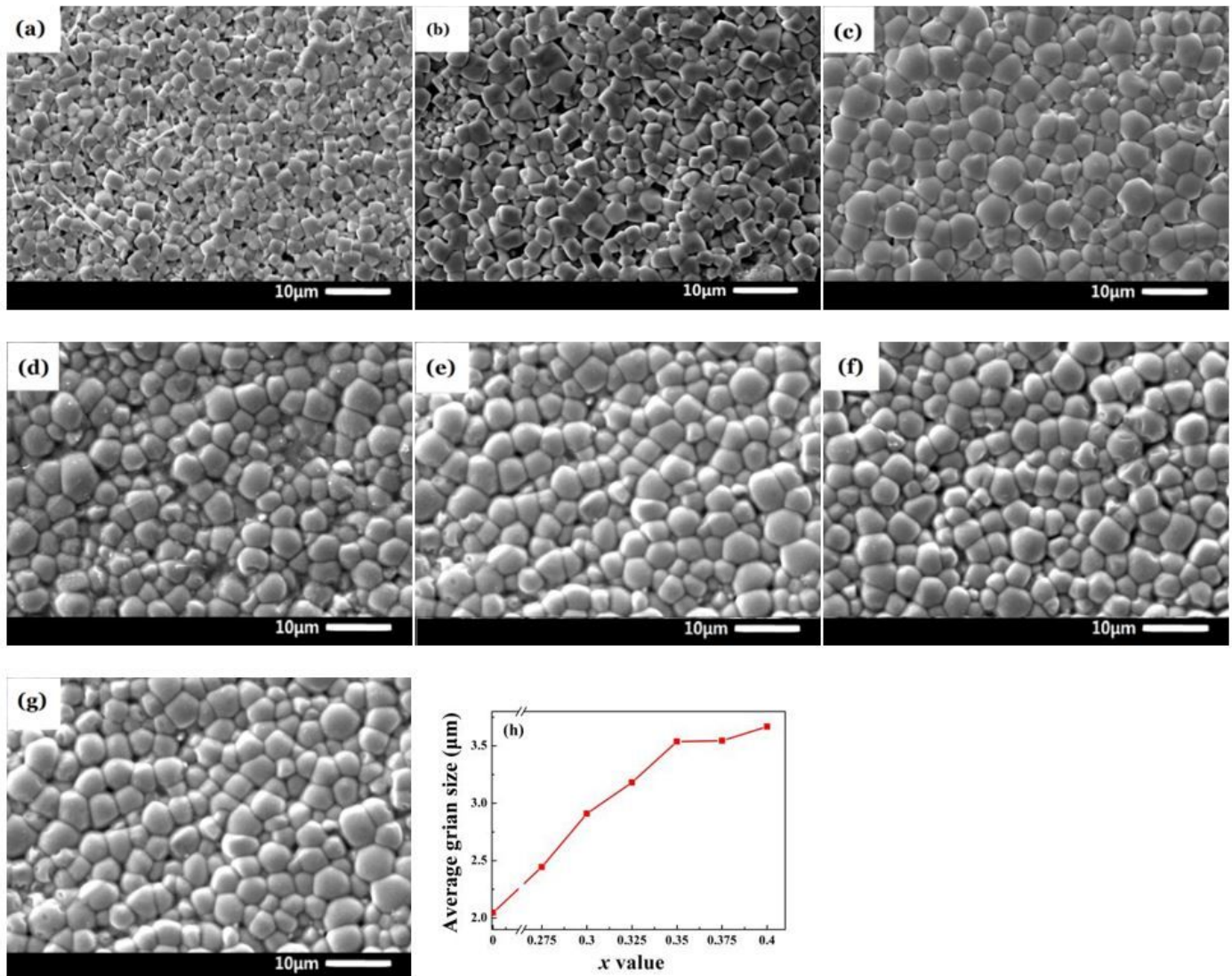


Figure 3

The SEM images of $(1-x)\text{Bi}_{0.85}\text{Nd}_{0.15}\text{Fe}_{0.98}\text{Zr}_{0.02}\text{O}_3 - x\text{BaTiO}_3$ ceramics: (a) $x = 0$, (b) $x = 0.275$, (c) $x = 0.3$, (d) $x = 0.325$, (e) $x = 0.35$, (f) $x = 0.375$, (g) $x = 0.4$, (h) average grain size.

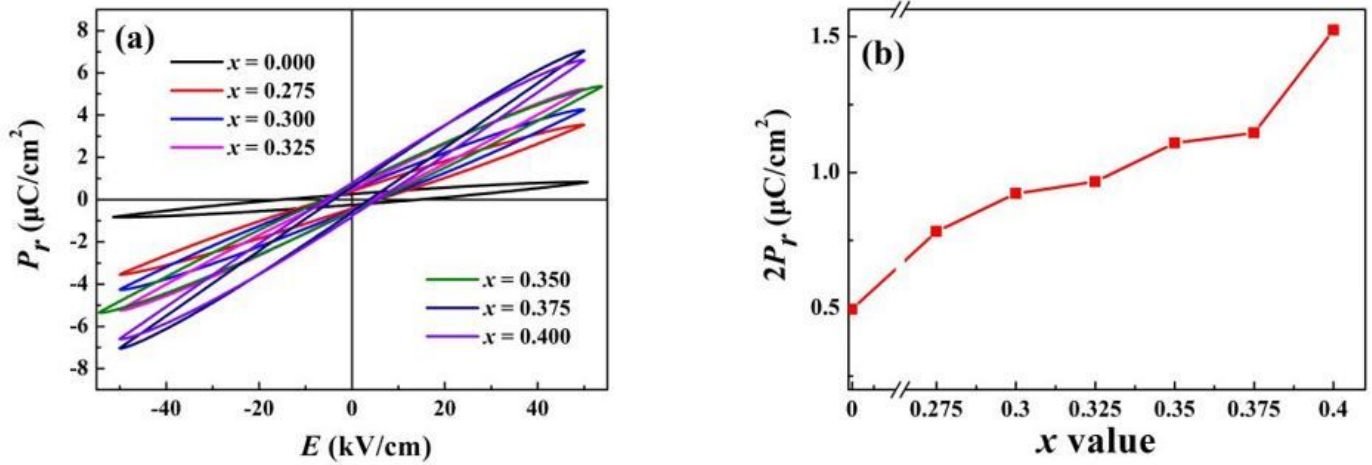


Figure 4

(a) P-E loops of $(1-x)\text{Bi}_{0.85}\text{Nd}_{0.15}\text{Fe}_{0.98}\text{Zr}_{0.02}\text{O}_3-x\text{BaTiO}_3$ ($x = 0, 0.275, 0.3, 0.325, 0.35, 0.375$ and 0.4) ceramics at room temperature (b) remnant polarization ($2P_r$) as a function of x .

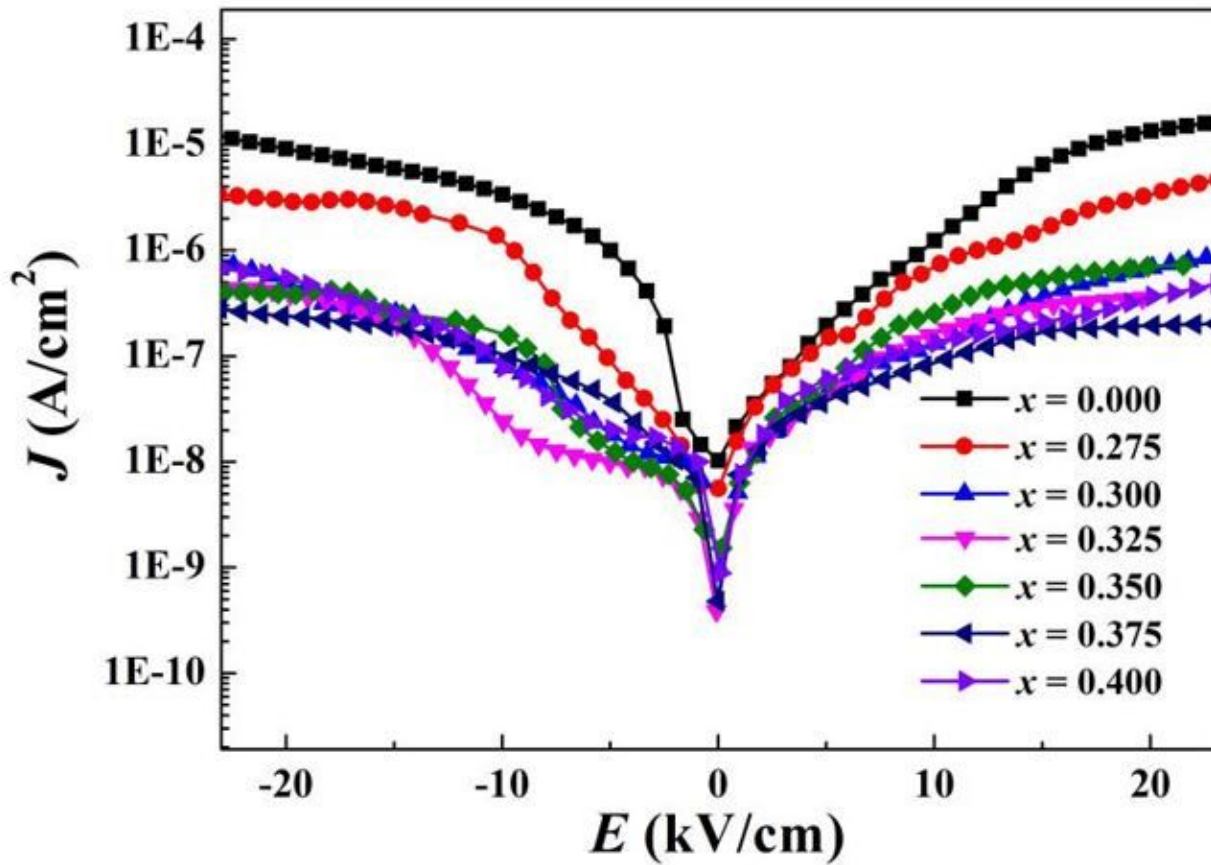


Figure 5

Leakage current density J of $(1-x)\text{Bi}_0.85\text{Nd}_0.15\text{Fe}_0.98\text{Zr}_0.02\text{O}_3-x\text{BaTiO}_3$ ($x = 0, 0.275, 0.3, 0.325, 0.35, 0.375$ and 0.4) ceramics as a function of electric field E .

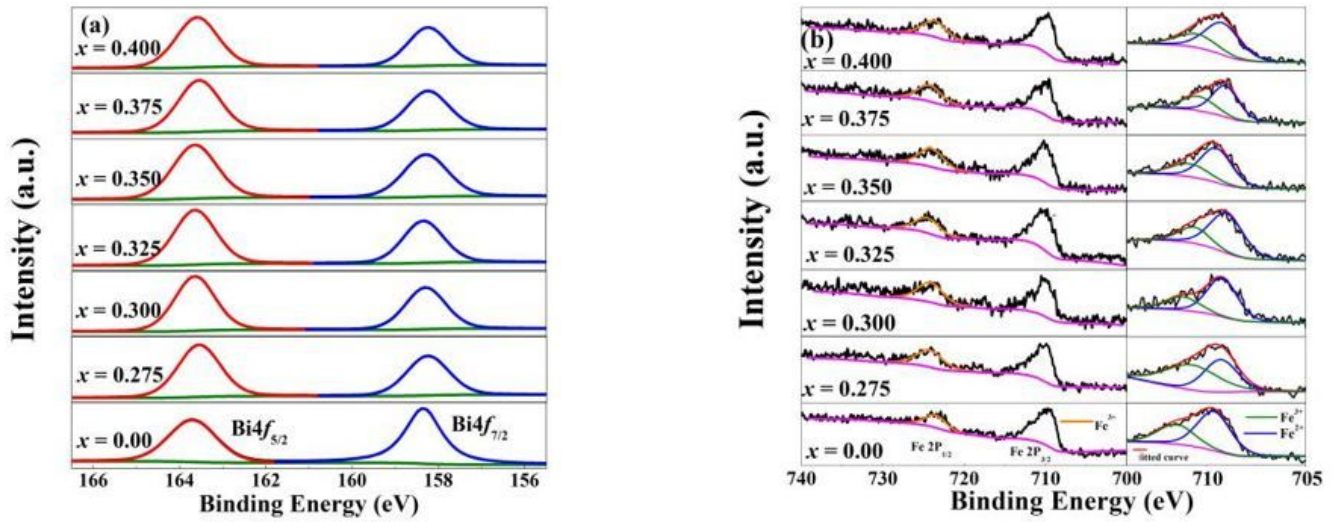


Figure 6

XPS results of the (a) Bi 4f and (b) Fe 2p lines of $(1-x)\text{Bi}_0.85\text{Nd}_0.15\text{Fe}_0.98\text{Zr}_0.02\text{O}_3-x\text{BaTiO}_3$ ($x = 0, 0.275, 0.3, 0.325, 0.35, 0.375$ and 0.4) ceramics.

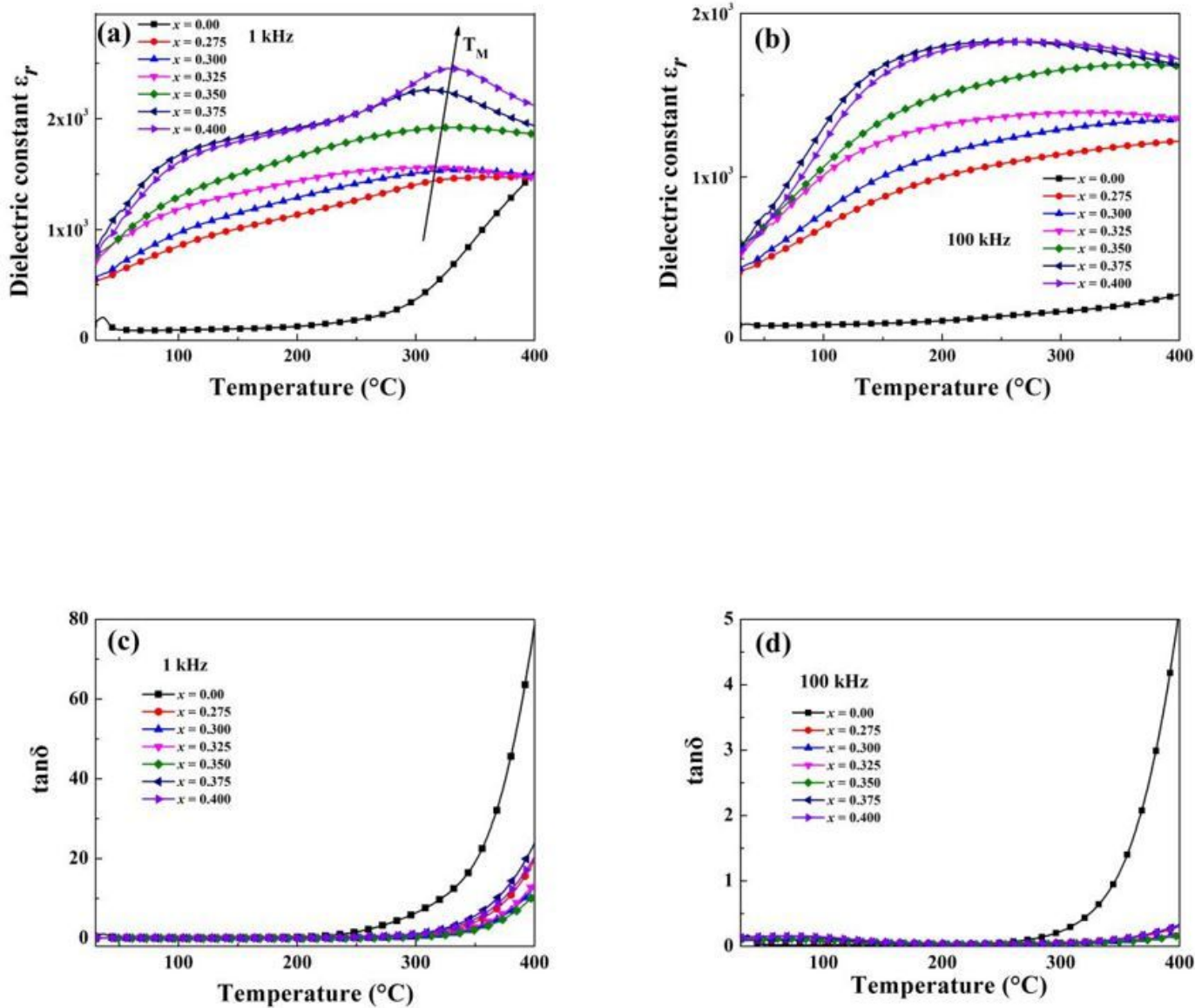


Figure 7

Temperature dependence of dielectric constant (ϵ_r) (a) 1 kHz, (b) 100 kHz and dielectric loss ($\tan\delta$) (c) 1 kHz, (d) 100kHz for $(1-x)\text{Bi}_{0.85}\text{Nd}_{0.15}\text{Fe}_{0.98}\text{Zr}_{0.02}\text{O}_{3-x}\text{BaTiO}_3$ ($x = 0, 0.275, 0.3, 0.325, 0.35, 0.375$ and 0.4) ceramics.

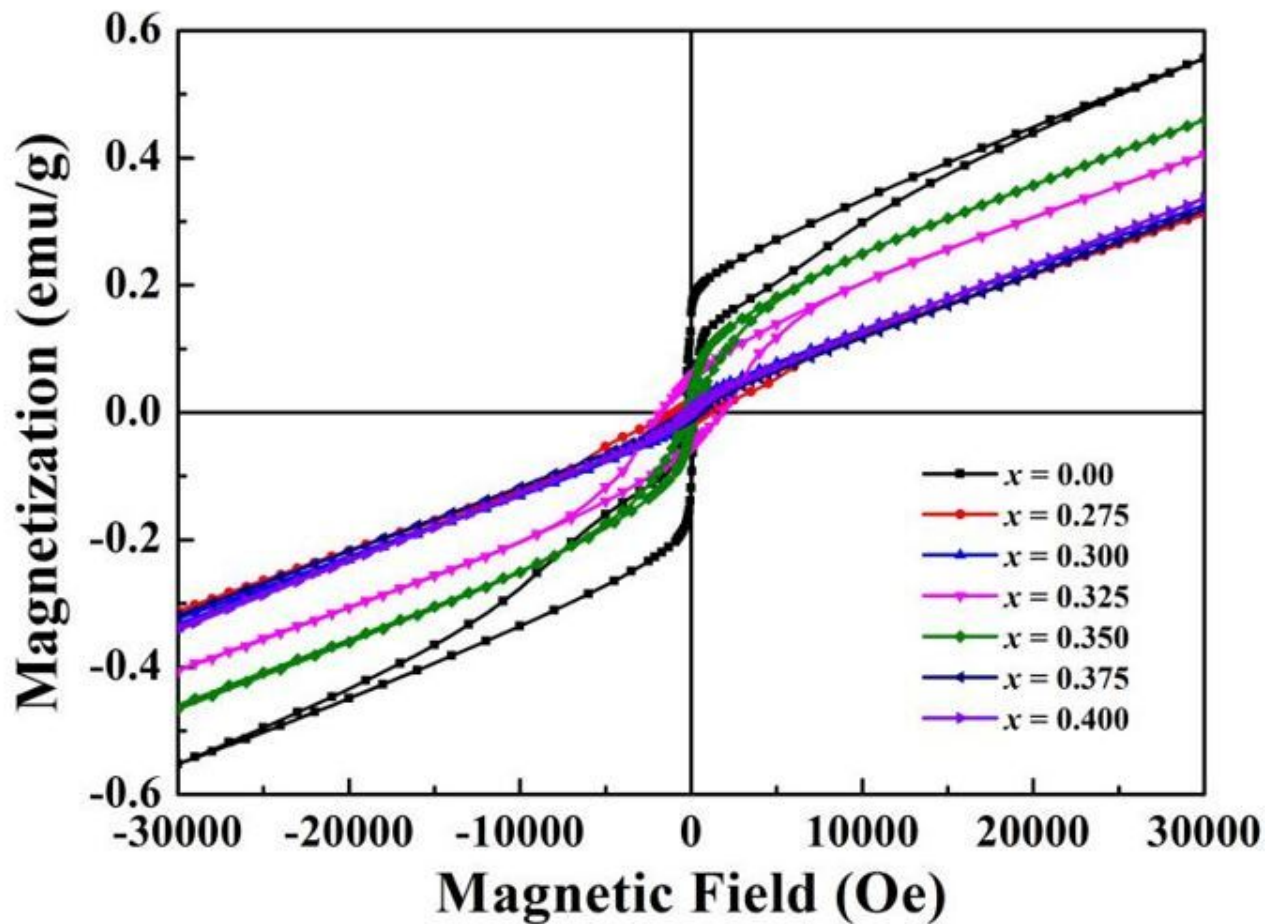


Figure 8

Magnetic hysteresis loops of $(1-x)\text{Bi}_{0.85}\text{Nd}_{0.15}\text{Fe}_{0.98}\text{Zr}_{0.02}\text{O}_3-x\text{BaTiO}_3$ ($x = 0, 0.275, 0.3, 0.325, 0.35, 0.375$ and 0.4) ceramics at room temperature.